Structural Engineering and Mechanics, *Vol. 98, No. 1 (2026) 77-92*
https://doi.org/10.12989/sem.2026.98.1.077

Techno-Press

Full-field strain reconstruction of BWB aircraft structures using mode superposition-based virtual sensing

Mincheol Shin[1], Sungbo Lee[**2], Seongpil Cho[*1]

[1]Department of Aerospace and Mechanical Engineering, Korea Aerospace University, 76 Hanggongdaehak-ro, Deogyang-gu, Goyang, Gyeonggi 10540, Republic of Korea
[2]Gen-IV Reactor Technology Development Division, Korea Atomic Energy Research Institute, 111 Daedeok-daero, 989beon-gil, Yuseong-gu, Daejeon 34057, Republic of Korea

(Received January 30, 2026, Revised March 7, 2026, Accepted March 11, 2026)

Abstract. The ability to accurately estimate structural responses is essential for ensuring safety and enabling early damage detection in complex engineering systems. However, obtaining full-field structural state data is often hindered by the physical limitations of sensor installation in extreme operational environments and the scarcity of failure data required for data-driven approaches. To address these challenges, this paper proposes a physics-based virtual sensing technique that reconstructs the full-field strain distribution using a sparse array of strain sensors. The proposed method utilizes the mode superposition principle, approximating the global structural response as a linear combination of modal weights derived from limited sensor data. A key feature of this approach is the construction of a hybrid basis set that integrates dominant low-order eigenmodes with quasi-static correction vectors, ensuring that both dynamic characteristics and static aeroelastic deformations are accurately captured with high computational efficiency. The method is applied to a blended wing body (BWB) aircraft structure, and its performance is verified through numerical simulations under various cruise conditions with elliptical lift distributions. The analysis results show that the proposed technique effectively estimates the strain field over the entire structure. Relative errors are mostly within 10% compared to the finite element analysis reference value. In addition, the error is less than 4% in the major deformation area, showing high precision. These findings confirm the potential of the proposed virtual sensing framework as a robust and efficient solution for real-time structural health monitoring in aerospace applications.

Keywords: blended wing body; finite element analysis; full-field strain reconstruction; mode superposition method; virtual sensing

1. Introduction

Engineering structures are inevitably exposed to complex dynamic loading regimes throughout their service lives, rendering the continuous monitoring of structural deformation imperative for safety assurance. Accurate assessment of such structural behaviors provides critical insights into the system's integrity and potential failure mechanisms [1]. Consequently, structural health monitoring (SHM) technologies, which measure structural response states in real time, are

---

*Corresponding author, Professor, E-mail: spcho@kau.ac.kr
**Co-corresponding author, Ph.D., E-mail: sblee4724@kaeri.re.kr

http://www.techno-press.org/sem/5
ISSN: 1225-4568 (Print), 1598-6217 (Online)

considered essential for early damage detection and maintenance of structures [2, 3]. However, structures operating in extreme environments often have technical limitations in directly measuring structural response states due to constraints on physical access and harsh environmental conditions [4-7].

To overcome these limitations, recent research in structural dynamics and health monitoring has explored structural state identification techniques. Previous studies have proposed various methodologies, such as inverse load identification methods [8, 9] and Kalman filter-based approaches [10, 11], to estimate structural response states. In parallel with these estimation techniques, advanced data-driven approaches have been widely adopted for anomaly detection in complex systems [12, 13].

Despite these advancements, significant challenges remain. Inverse load identification methods often face challenges due to the ill-posed nature of the problem, making them highly sensitive to measurement noise and modeling errors. Furthermore, while Kalman filter-based approaches offer high accuracy, their computational cost scales prohibitively with the dimensionality of the model, often limiting their utility for real-time monitoring of large-scale structures without model order reduction. Similarly, data-driven methods, such as deep neural networks, require vast amounts of training data representing various damage scenarios, which are practically impossible to obtain for complex engineering systems such as aircraft, offshore structures, wind turbines, and power plants.

These limitations are particularly critical for aircraft structures, which possess complex characteristics formed by numerous components and operate under extreme environmental conditions, including severe temperature changes and aerodynamic loads. Such environments carry a high potential for inducing fatigue damage in the structure, necessitating advanced detection technology to prevent accidents and ensure structural integrity and safety [14-17]. In particular, accurate fatigue life estimation necessitates not only localized sensor data but also full-field response reconstruction across the entire structure over time [18, 19].

In practice, installing physical sensors like strain gauges and accelerometers on operational aircraft is challenging. Even when installed, these sensors provide only localized information, and the reliability of the observed data may be compromised under severe conditions [20-22]. To address these challenges, virtual sensing technology has emerged as a promising solution [23-28]. Virtual sensing is an indirect measurement method that estimates structural response states in uninstrumented areas based on data acquired from a sparse set of physical sensors. Previous studies have demonstrated the validity of these techniques by comparing estimated data with actual sensor data under various dynamic loads [18-20, 28]. However, these validations have predominantly been confined to simplified, idealized structural geometries, such as one-dimensional beams or two-dimensional plates. The direct translation of these methods to highly complex, built-up aircraft structures remains a significant engineering challenge.

In this context, this paper proposes an advanced application of a virtual sensing technique capable of reconstructing the full-field strain distribution of a three-dimensional blended wing body (BWB) aircraft structure. Unlike purely data-driven approaches, the proposed method combines a physics-based finite element (FE) model with sparse sensor data using mode superposition theory [18, 26-28]. Moving beyond the simplified geometries of prior studies, the analyzed BWB model incorporates structurally practical representative members, including spars and ribs, which introduce spatially varying stiffness distributions, complex internal load transfer paths. Validating the numerical stability and reconstruction performance under such complex structural conditions is a crucial step toward real-world aircraft applications. Fig. 1 illustrates the overall procedure. The process begins with the creation of a FE model and the selection of a basis

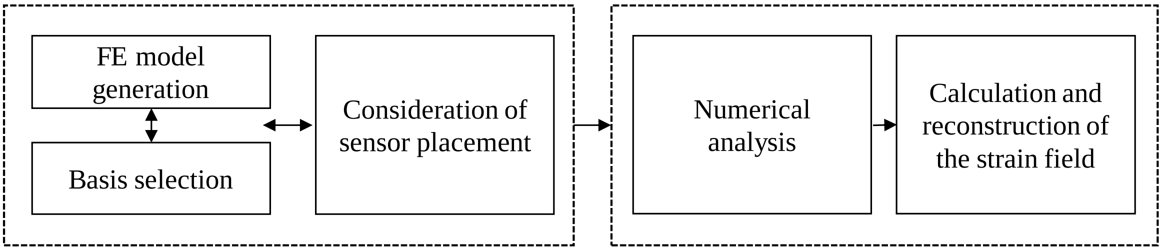

Figure 1. Flowchart of the proposed virtual sensing technique based on mode superposition method

that effectively simulates the dynamic behavior. Based on this, sensor locations are determined to ensure estimation accuracy [28]. Subsequently, numerical analysis is performed to obtain local response data, which is then combined with the mode superposition algorithm to reconstruct the strain field of the entire structure. For validation, the strain calculated via finite element analysis (FEA) is treated as the reference to assess the accuracy and feasibility of the developed algorithm.

The remainder of this article is organized as follows. Section 2 introduces the formulation of virtual sensing algorithms. Section 3 details the numerical simulations using the BWB aircraft model. Section 4 presents the conclusions.

2. Formulation of virtual sensing algorithms

This section outlines the finite element method-based formulation process that serves as the theoretical foundation for implementing virtual sensing strategies. The dynamic behavior of structures is governed by the equations of motion for multi-degree-of-freedom systems. In this study, the mode superposition method is applied to approximate the structural response, ensuring both computational efficiency and physical validity. The procedure for constructing the strain mode matrix and the mathematical algorithm for reconstructing the full-field strain from limited sensor data are detailed below.

2.1 Structural dynamics and strain mode

To implement virtual sensing techniques, displacement basis vectors must initially be constructed using FEA. Eq. (1) represents the equation of motion for the FE model:

$$\mathbf{M}\ddot{\mathbf{U}}(t) + \mathbf{C}\dot{\mathbf{U}}(t) + \mathbf{K}\mathbf{U}(t) = \mathbf{F}(t) \tag{1}$$

where $\mathbf{M}$, $\mathbf{C}$, and $\mathbf{K}$ denote the mass matrix, damping matrix, and stiffness matrix, respectively. $\mathbf{U}$, $\dot{\mathbf{U}}$, and $\ddot{\mathbf{U}}$ are the displacement, velocity and acceleration vectors, and $\mathbf{F}$ is the load vector. Generally, the equation of motion involves numerous degrees of freedom (DOFs), requiring substantial computational effort. To address this efficiency issue, the mode superposition theory is applied, allowing the displacement vector to be approximated as a linear combination of selected mode vectors. To obtain these vectors, the eigenvalue problem is solved to determine the mode shapes corresponding to the structure's natural frequencies [18, 28, 29]. The eigenvalue problem under free vibration conditions is expressed as Eq. (2):

$$[\mathbf{K} - \lambda_i \mathbf{M}]\mathbf{\Phi}_i = 0 \tag{2}$$

where λ_i denotes the eigenvalue, and $\boldsymbol{\Phi_i}$ is mode shape vector corresponding to that frequency. The accuracy of the mode superposition method relies fundamentally on the selection of a basis set that adequately spans the actual deformation space. In structural dynamics, higher-order modes typically contribute to localized high-frequency deformations but possess low participation factors in the global strain energy distribution under standard aerodynamic loads. Consequently, truncating the basis to a set of dominant low-order modes allows for a significant reduction in computational dimensionality without compromising global estimation accuracy. However, to account for the residual flexibility of the omitted high-frequency modes, incorporating quasi-static correction vectors is often necessary [18]. This ensures that the steady-state response under static loads is accurately captured, bridging the gap between dynamic approximation and static reality. Consequently, the displacement response of the structure can be approximated using a truncated set of modes rather than full DOFs, as shown in Eq. (3). Furthermore, using the strain-displacement relationship, the strain state response can be derived as shown in Eq. (4):

$$\mathbf{U}(t) \approx \sum_{i=1}^{N} \boldsymbol{\Phi}_i q_i(t) = \boldsymbol{\Phi}\mathbf{q}(t) \tag{3}$$

$$\boldsymbol{\varepsilon}(t) \approx \sum_{i=1}^{N} \boldsymbol{\Psi}_i q_i(t) = \boldsymbol{\Psi}\mathbf{q}(t) \tag{4}$$

where $\boldsymbol{\Phi} = [\boldsymbol{\Phi}_1\ \boldsymbol{\Phi}_2\ \cdots\ \boldsymbol{\Phi}_N]$ denotes the displacement mode matrix, $\boldsymbol{\Psi} = [\boldsymbol{\Psi}_1\ \boldsymbol{\Psi}_2\ \cdots\ \boldsymbol{\Psi}_N]$ is the strain mode matrix, N is the number of selected modes, and $\mathbf{q}(\boldsymbol{t}) = [\boldsymbol{q_1}(\boldsymbol{t})\ \boldsymbol{q_2}(\boldsymbol{t})\ \cdots\ \boldsymbol{q_N}(\boldsymbol{t})]^{\boldsymbol{T}}$ represents the modal coordinates (mode contribution). Thus, the dynamic response of a structure can be effectively approximated using a subset of its mode vectors [28].

2.2 Strain field reconstruction algorithm

The proposed algorithm aims to reconstruct the strain field for the entire structure using data from a limited number of sensors. The sensor data ($\boldsymbol{\varepsilon_m}$) is obtained from FEA (reference) at specific sensor locations.

$$\boldsymbol{\varepsilon}_m = \left[\varepsilon_{m,1}\ \varepsilon_{m,2}\ \cdots\ \varepsilon_{m,n}\right]^T \tag{5a}$$

$$\bar{\boldsymbol{\varepsilon}}_p = \left[\bar{\varepsilon}_{p,1}\ \bar{\varepsilon}_{p,2}\ \cdots\ \bar{\varepsilon}_{p,n}\right]^T \tag{5b}$$

where $\boldsymbol{\varepsilon_m}$ denotes the strain measured by the sensors and $\bar{\boldsymbol{\varepsilon}}_{\boldsymbol{p}}$ is the estimated strain at the sensor locations using mode superposition, as defined in Eq. (5). The error between the measured and estimated strain is defined using least squares method as follows:

$$\sum_{i=1}^{n}\left(\bar{\varepsilon}_{p_i} - \varepsilon_{m_i}\right)^2 = \left(\bar{\boldsymbol{\varepsilon}}_p - \boldsymbol{\varepsilon}_m\right)^T\left(\bar{\boldsymbol{\varepsilon}}_p - \boldsymbol{\varepsilon}_m\right) = (\boldsymbol{\Psi}_m\mathbf{q}(t) - \boldsymbol{\varepsilon}_m)^T(\boldsymbol{\Psi}_m\mathbf{q}(t) - \boldsymbol{\varepsilon}_m) \tag{6}$$

where $\boldsymbol{\Psi_m}$ represents the partial strain mode matrix corresponding only to the sensor locations, extracted from the full matrix $\boldsymbol{\Psi}$. To minimize the difference between the measured and the estimated strain data, the optimal mode contribution $\hat{\mathbf{q}}(t)$ is derived by minimizing Eq. (6) with respect to $\mathbf{q}(t)$:

$$\hat{\mathbf{q}}(t) = (\boldsymbol{\Psi}_m^T \boldsymbol{\Psi}_{\boldsymbol{m}})^{-1} \boldsymbol{\Psi}_m^T \boldsymbol{\varepsilon}_m \tag{7}$$

where $\hat{\mathbf{q}}(t)$ refers to the reconstructed modal contribution. Finally, the full-field displacement and strain can be reconstructed using the full mode matrices ($\boldsymbol{\Phi}$ and $\boldsymbol{\Psi}$) and the estimated modal coordinates:

$$\mathbf{U}_p(t) \approx \sum_{i=1}^{N} \boldsymbol{\Phi}_i \hat{q}_i(t) = \boldsymbol{\Phi}\hat{\mathbf{q}}(t) \tag{8}$$

$$\bar{\boldsymbol{\varepsilon}}_p(t) \approx \sum_{i=1}^{N} \boldsymbol{\Psi}_i \hat{q}_i(t) = \boldsymbol{\Psi}\hat{\mathbf{q}}(t) \tag{9}$$

As a result, the reconstructed displacement and strain fields are derived through a linear combination of the reconstructed modal contribution and the displacement mode shape matrices.

3. Numerical simulation using the BWB aircraft model

3.1 Finite element model of the BWB aircraft

This study investigates the BWB configuration, which is emerging as a promising platform for next-generation aircraft. Fig. 2 shows the configuration of the BWB aircraft model used in the analysis. Unlike the traditional tube and wing (TAW) configuration, it is characterized by a unified structure where the fuselage and wing are merged with smooth curves. This geometric configuration enables the entire structure to function as a single lift-generating body, providing structural and aerodynamic advantages in terms of improved aerodynamic performance and maximized fuel efficiency [30-32].

To generate a reliable displacement basis, a FE model was constructed to accurately represent the structure's physical characteristics. Considering the structural symmetry, a FE model based on 3-node shell elements was constructed for half the geometry of the BWB aircraft model, as shown in Fig. 3. The model consists of a total of 13,670 elements and 6,426 nodes, with 38,556 total degrees of freedom. Clamped boundary conditions constraining all 6 degrees of freedom were

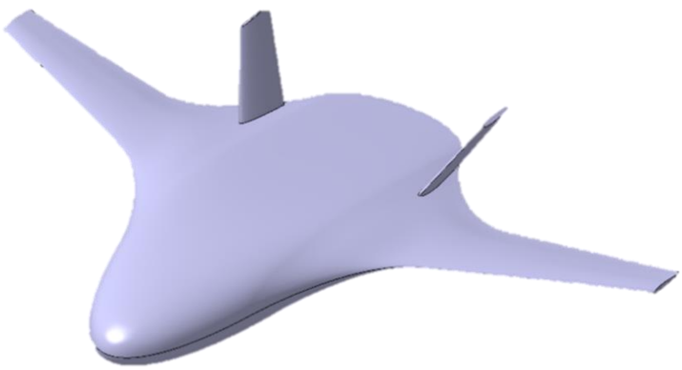

Figure 2. Geometric configuration of the blended wing body (BWB) aircraft model [33]

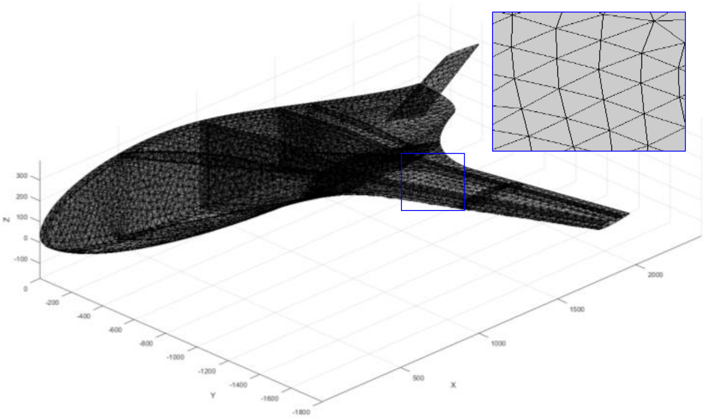

Figure 3. Finite element model of the BWB aircraft structure

Table 1. Material properties of aluminum 6061-T6 and polycarbonate

Aluminum 6061-T6	*E* (MPa)	68,900
	v	0.33
	ρ (kg/m^3)	2,700
Polycarbonate	*E* (MPa)	2,300
	v	0.37
	ρ (kg/m^3)	1,200

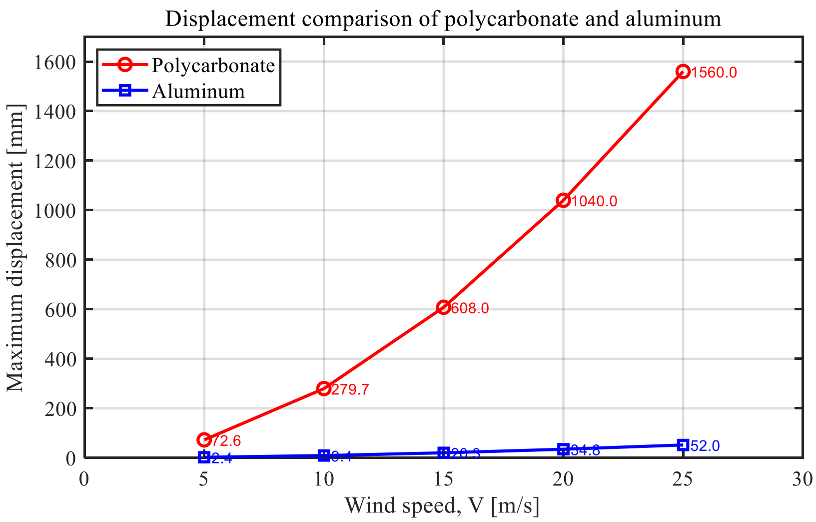

Figure 4. Comparison of maximum wing tip displacement for material selection suitability

applied to the end regions of the fuselage section. Polycarbonate was selected as the structural material for this analysis, with its properties compared with Aluminum 6061-T6 in Table 1. While distinct from standard aerospace-grade metals, polycarbonate was employed to enhance strain measurability, facilitating effective analysis of the strain distribution. As illustrated in Fig. 4, the

Table 2. Specifications of the BWB scaled prototype

Specification	Values
Fuselage length (m)	2.42
Wing span (m)	3.6
Wing area (m^2)	3.15
Wing loading (kg/m^2)	7.6
Maximum take-off weight (kg)	24
Maximum lift-drag ratio (-)	12

low elastic modulus of polycarbonate induces significant displacement at the wing tip under the applied lift loads. This material selection ensures that the structural deformation is sufficiently large to be captured by sensors, facilitating effective validation of the strain estimation algorithm even under laboratory-scale loading conditions.

3.2 Aerodynamic load conditions

This study evaluated the structural response of the BWB aircraft under varying speeds by defining five distinct analysis conditions. Assuming quasi-static cruise conditions at steady flight velocities of 5, 10, 15, 20, and 25 m/s, the lift loads acting on the BWB aircraft were derived based on the scaled prototype specifications [34, 35]. Table 2 presents the scaled prototype specifications for the BWB aircraft model.

To calculate the lift distribution, the aerodynamic circulation concept was applied, and considering induced drag minimization, the circulation distribution along the span direction was assumed to be elliptical, as shown in Eq. (10).

$$\Gamma(y) = \Gamma_0 \sqrt{1 - \left(\frac{2y}{b}\right)^2} \tag{10}$$

where, $\Gamma(y)$ represents the circulation distribution along the spanwise coordinate y, and Γ_0 is the circulation at the mid-body and b is the spanwise length.

Subsequently, the total lift coefficient is defined in terms of circulation by Eq. (11a), and the lift per unit span length is defined by Eq. (11b).

$$C_L = \int_0^{b/2} \frac{2\Gamma(y)}{V_\infty \bar{c}} d\left(\frac{2y}{b}\right) \tag{11a}$$

and

$$c(y)C_l(y)/\bar{c} = 2\Gamma(y)/V_\infty \bar{c} \tag{11b}$$

where C_L is the lift coefficient, V_∞ is the free-stream velocity, $c(y)$ is the local chord length at spanwise position y, $C_l(y)$ is the section lift coefficient, $\bar{c}$ is the mean chord length.

By combining the equations above, the lift load distribution along the unit length direction is ultimately defined as shown in Eq. (12) [36].

$$L'(y) = \frac{1}{2}\rho V_\infty^2 c(y) C_l(y) \tag{12}$$

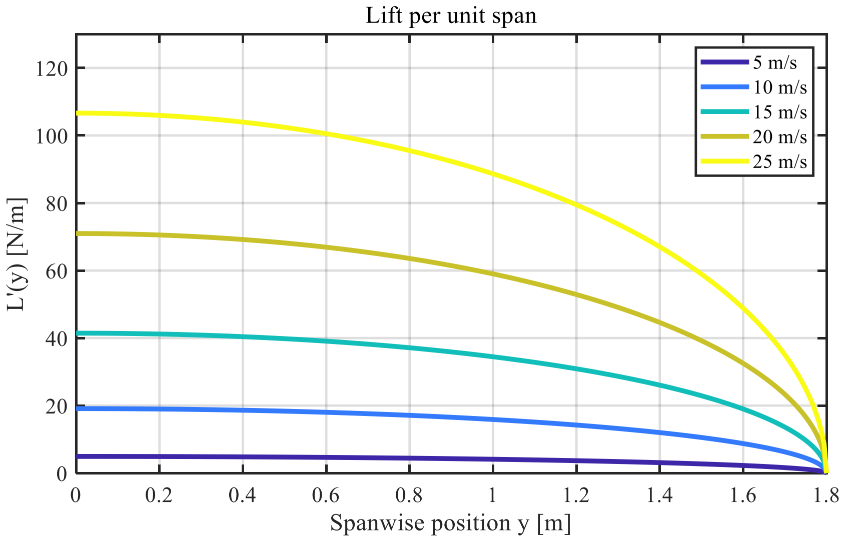

Figure 5. Elliptical lift distribution per unit span calculated for varying cruise speeds

where $L'(y)$ denotes the lift distribution per unit span length and ρ is the air density.

In this study, an ideal elliptical lift distribution was assumed to simulate the cruise condition. While actual flight loads involve complex non-linear aerodynamic phenomena arising from angle of attack variations and gusts, this simplified static load model provides a deterministic baseline for evaluating the reconstruction algorithm's performance. The primary objective of this study is to verify the virtual sensing capability under known loading conditions rather than to model exact flight dynamics. The resulting lift distribution at each point is shown in Fig. 5, and this load distribution was applied as the quasi-static load during the FEA. Therefore, the quasi-static deformation shapes induced by the lift loads were derived from the FEA and used as the reference deformation fields for validating the proposed virtual sensing technique.

3.3 Basis selection and sensor placement

To ensure high estimation accuracy, it is essential to select a basis that effectively represents the structural characteristics under operating loads. Therefore, a parametric sensitivity analysis was conducted to evaluate the impact of these variables on reconstruction accuracy. By varying the number of retained eigenmodes and input sensors, the reconstruction error was systematically assessed. As shown in Fig. 6, the analysis revealed that the lowest normalized root mean square (NRMS) error was achieved when 11 eigenmodes were retained. Furthermore, the accuracy improvements became marginal beyond 12 sensors. Consequently, considering both the reconstruction performance and practical constraints such as sensor installation cost and system complexity, an optimal configuration of 11 eigenmodes and 12 sensors was determined.

Based on these findings, the displacement basis was constructed by combining the lowest 11 eigenmodes derived from the modal analysis with the quasi-static deformation shapes obtained under cruise conditions. This basis set ensures that both the dynamic characteristics and the static aeroelastic deformation are captured effectively. The representative mode shapes (from the 1^{st} to the 5^{th} eigenmode) are illustrated in Fig. 7.

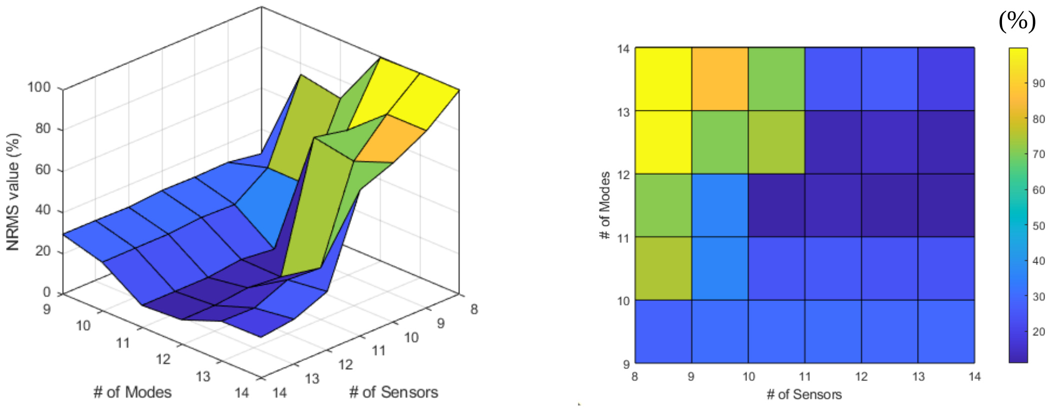

Figure 6. Reconstruction error evaluated as a function of the number of retained eigenmodes and input sensors

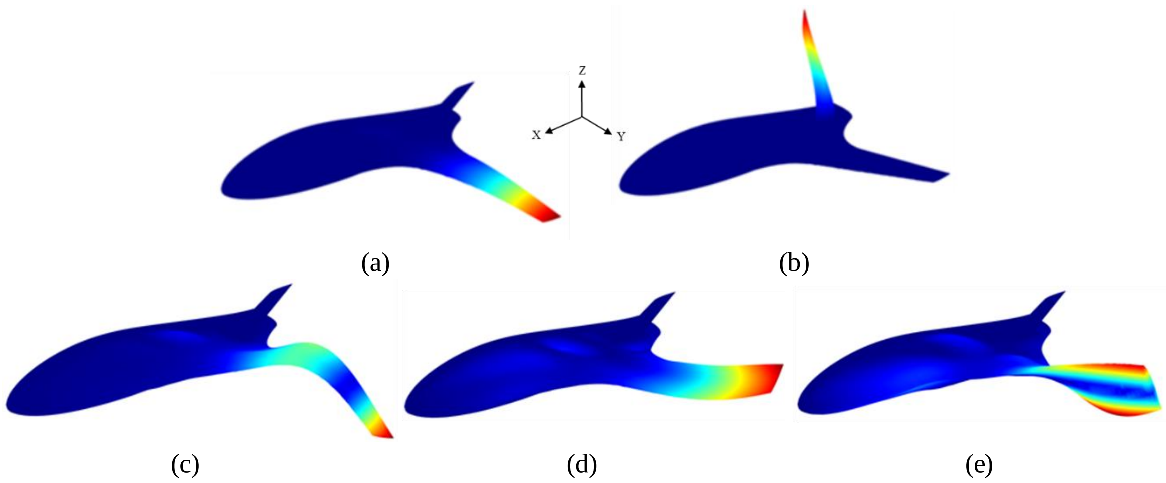

Figure 7. Dominant mode shapes and natural frequencies of the BWB structure: (a) 1st mode (14.15 Hz), (b) 2nd mode (45.54 Hz), (c) 3rd mode (55.25 Hz), (d) 4th mode (72.56 Hz), and (e) 5th mode (83.03 Hz)

To measure the structural response state under operational conditions, the 12 selected strain measurement sensors were positioned on the finite element (FE) model. Specifically, 6 sensors were placed on the upper skin and 6 on the lower skin of the fuselage. The fuselage region was chosen to circumvent the practical limitations associated with instrumenting the wing surfaces. In particular, direct sensor installation on the wing, especially at the leading and trailing edges, is severely constrained by high surface curvature, limited internal access for cabling, and the critical requirement to maintain a smooth aerodynamic profile. Consequently, positioning sensors on the fuselage serves as a practical alternative that minimizes aerodynamic interference on the lifting surfaces while providing a stable baseline for estimating the global deformation behavior.

In this study, the term "full-field" refers to the reconstructed structural response over the entire FE mesh. While the proposed algorithm estimates the continuous displacement and strain distributions across the entire BWB structure, the quantitative accuracy of this full-field estimation is verified at discrete locations. Accordingly, 8 evaluation points were defined at the leading and

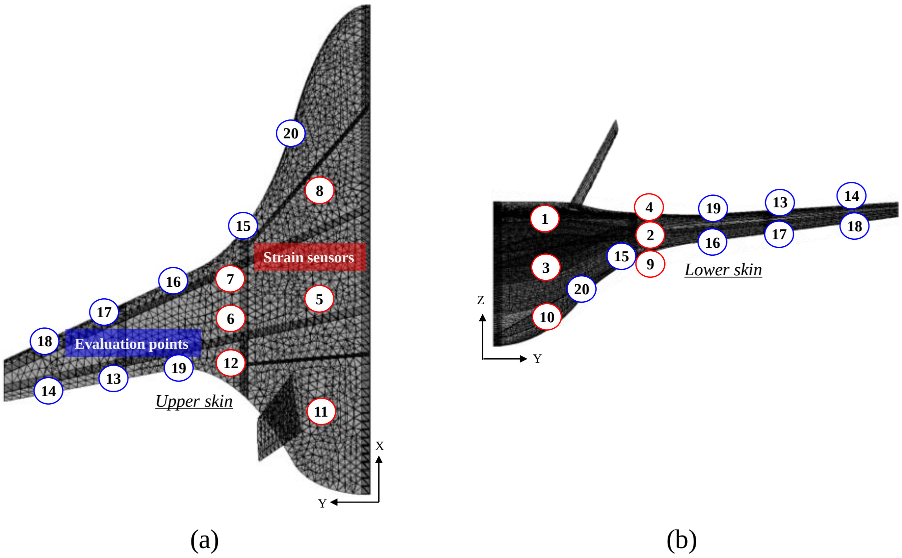

Figure 8. Sensor placement strategy on the finite element model: (a) Plan view and (b) Front view showing strain sensors (fuselage) and evaluation points (wing)

trailing edges of the wing. These locations were chosen because physical sensor installation is typically challenging in these regions due to aerodynamic constraints, yet significant structural deformation occurs there. The final determined configuration of the measurement sensors and the evaluation points is depicted in Fig. 8.

Based on this configuration, the strain values calculated from the FEA at the fuselage locations were utilized as input data for the proposed algorithm. These data are combined with the selected basis to reconstruct the strain field across the entire structure. The estimation accuracy is then evaluated by comparing the reconstructed results with the reference FEA data at the evaluation points on the wing.

3.4 Numerical validation

Numerical analysis was performed using strain data obtained from the selected displacement basis and sensor locations to evaluate the estimation performance of the proposed method. To simulate realistic measurement environments and assess the robustness of the algorithm against measurement uncertainty, artificial Gaussian white noise was introduced to the input sensor data. Specifically, noise with a standard deviation corresponding to 5% of the nominal strain magnitude was added to the FEA-extracted strain values at each sensor location, reflecting typical noise levels encountered in physical applications. The estimation accuracy at each evaluation point was quantified using the mean relative error, defined as follows:

$$\text{Mean relative error (\%)} = \frac{1}{N}\sum_{i=1}^{N}\left|\frac{\bar{\varepsilon}_p - \varepsilon_m}{\varepsilon_m}\right| \times 100 \tag{13}$$

where N is the number of data points, $\bar{\varepsilon}_p$ and ε_m represent the estimated and measured (reference) strain values, respectively. Fig. 9 shows the comparison between the strain data calculated by FEA

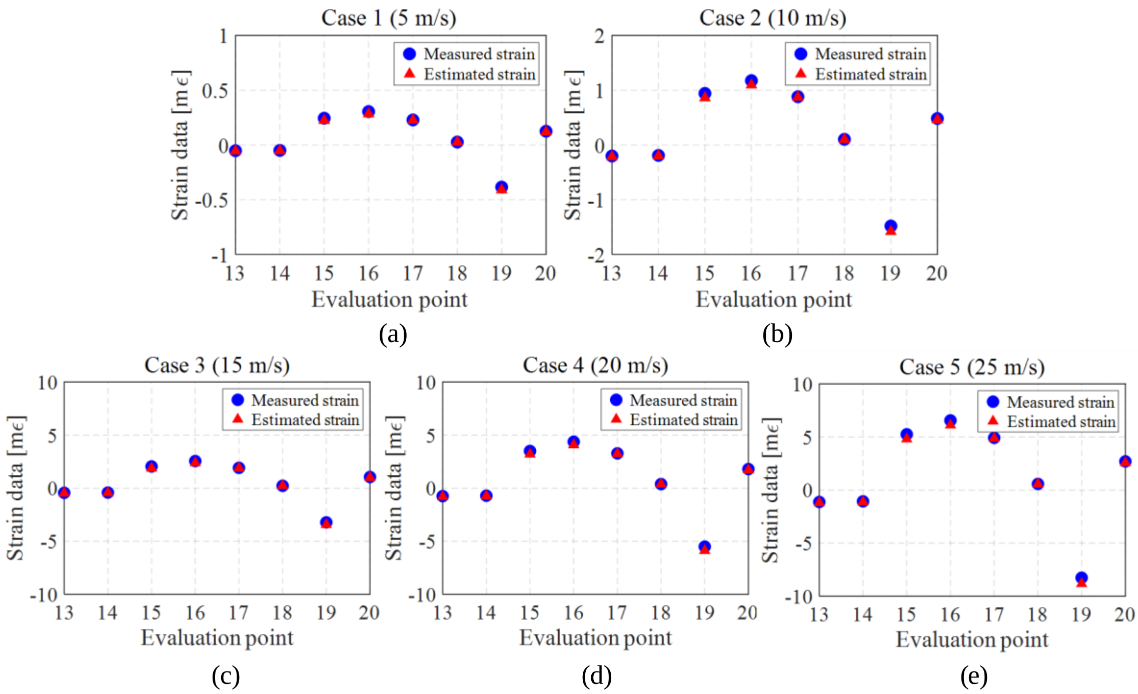

Figure 9. Comparison of reference (FEA) and estimated strain values at evaluation points under various flow velocities: (a) 5 m/s, (b) 10 m/s, (c) 15 m/s, (d) 20 m/s, and (e) 25 m/s

Table 3. Comparison between estimated strain and reference FEA data

No.	Case 1 (5 m/s)		Case 2 (10 m/s)		Case 3 (15 m/s)		Case 4 (20 m/s)		Case 5 (25 m/s)		Mean relative error (%)
	Est.*	Meas.*	Est.*	Meas.*	Est.*	Meas.*	Est.*	Meas.*	Est.*	Meas.*	
13	-0.056	-0.052	-0.216	-0.201	-0.469	-0.437	-0.803	-0.748	-1.204	-1.122	7.426
14	-0.052	-0.050	-0.202	-0.191	-0.438	-0.414	-0.749	-0.709	-1.124	-1.063	5.387
15	0.224	0.245	0.861	0.942	1.871	2.048	3.201	3.504	4.802	5.257	8.627
16	0.285	0.306	1.096	1.176	2.382	2.557	4.076	4.374	6.114	6.562	6.845
17	0.226	0.229	0.872	0.882	1.895	1.917	3.242	3.280	4.863	4.920	1.182
18	0.026	0.027	0.101	0.104	0.219	0.227	0.375	0.386	0.562	0.579	3.180
19	-0.411	-0.384	-1.582	-1.480	-3.440	-3.217	-5.884	-5.504	-8.827	-8.257	6.931
20	0.119	0.126	0.459	0.484	0.998	1.052	1.707	1.800	2.560	2.701	5.248

*Strain unit: millistrain (mε)

(reference) and the strain data estimated by the proposed method under these noisy conditions, evaluated at the specific points on the leading and trailing edges of the wing. The detailed numerical results and mean relative errors are listed in Table 3.

Comparing the reference strain at these evaluation points with the estimated strain revealed a trend where strain magnitude increased proportionally with increasing velocity. Across the five analysis conditions, the estimated results generally fell within an error range of 10% or less. These results confirm that the proposed virtual sensing technique can estimate structural response states

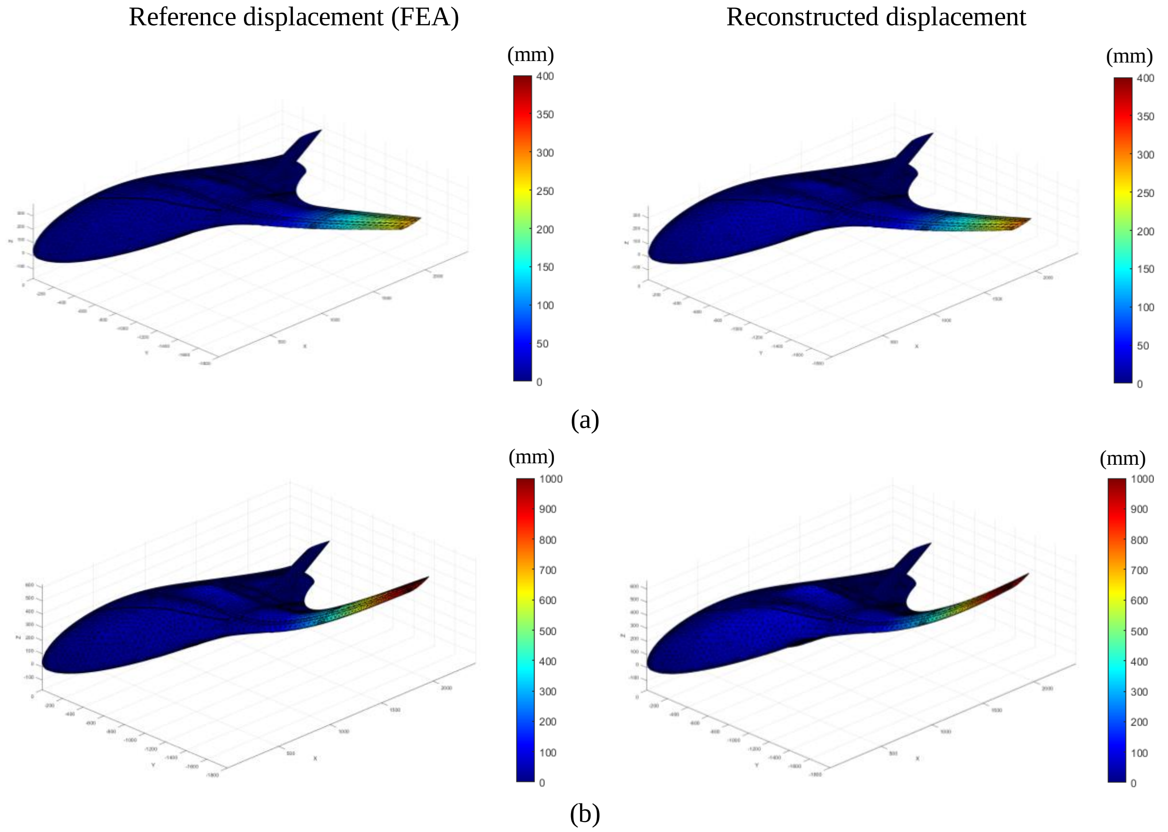

Figure 10. Displacement field reconstruction results: (a) 10 m/s cruise condition, (b) 20 m/s cruise condition

with high accuracy using only a limited number of sensors. In particular, evaluation points 17 and 18 showed a remarkably low error of 4% or less, demonstrating a high agreement with the reference strain data. Even for evaluation point 15, which showed a slightly elevated difference due to the steep strain gradients at the fuselage-wing transition, the result remained well within the target accuracy range.

Nevertheless, maintaining an overall error range within 10% indicates that the technique proposed in this study is reliable for estimating the structural response state. Furthermore, Fig. 10 shows the reconstructed full-field displacement results under representative analysis conditions of 10 m/s and 20 m/s cruise speed. Fig. 11 shows the corresponding full-field strain results. Compared to the reference FEA data, the estimated full-field results show highly consistent trends, even in the wing tip region where significant structural deformation occurs.

4. Conclusions

In this study, a virtual sensing technique based on the mode superposition method was proposed to reconstruct the global strain field of a blended wing body (BWB) aircraft structure. Unlike conventional aircraft, BWB aircraft structures are subjected to load conditions in which

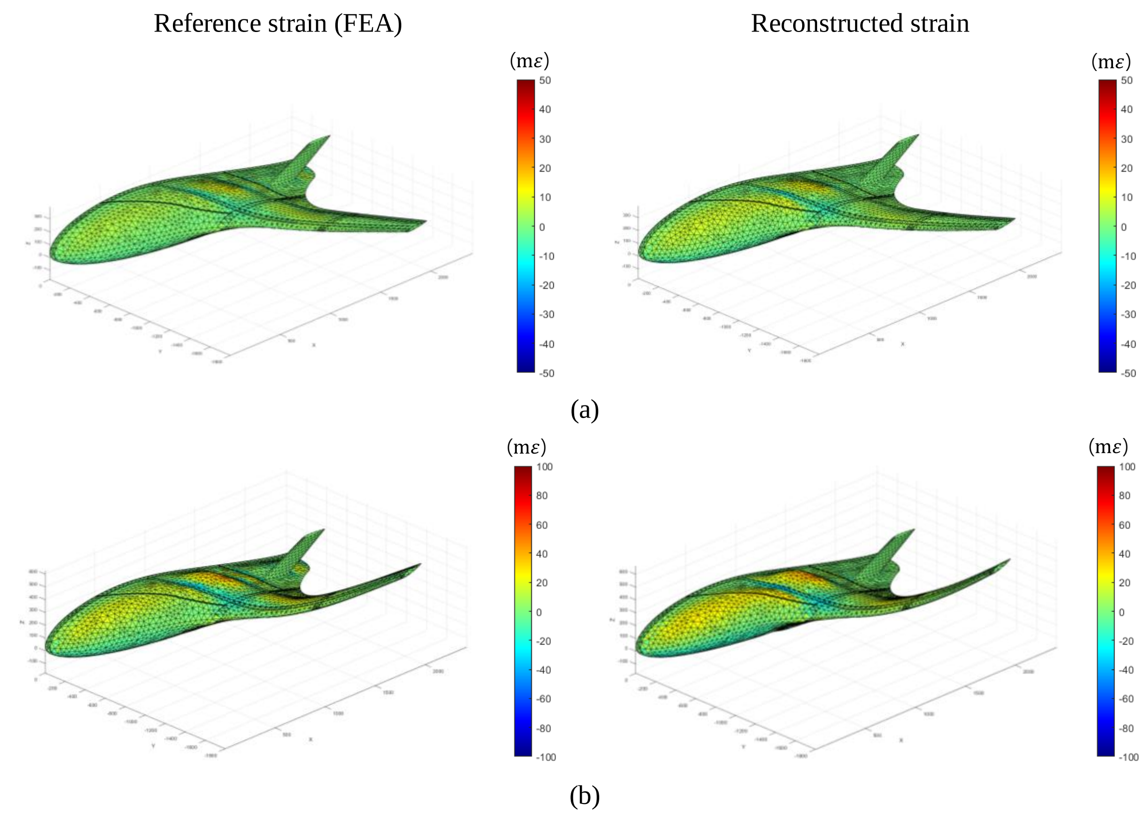

Figure 11. Strain field reconstruction results: (a) 10 m/s cruise condition, (b) 20 m/s cruise condition

aerodynamic loads interact with internal pressurized loads, so monitoring of all areas of the structure is important to ensure structural integrity. To this end, in this work, we formulated an algorithm that can efficiently reconstruct the behavior for the entire area of the structure using limited local strain data. By applying mode superposition theory, the structural response under operating conditions was reconstructed using a reduced basis of low-order modes, achieving a balance between computational efficiency and accuracy. To secure physical validity, a hybrid base was constructed by combining the quasi-static deformation shape derived from cruise conditions. Furthermore, through a parametric sensitivity analysis, an optimal configuration utilizing the lowest 11 eigenmodes and 12 strain sensors placed on the fuselage was determined. Numerical validation results show that the estimated strain values generally agree well with the reference finite element analysis results. In most cases, the error is within 10%. Notably, at certain evaluation points, the error is below 4%. The analysis results show that relatively large errors occur in regions with steep strain gradients. These areas correspond to structural transition zones, such as the fuselage-to-wing transition region. Therefore, they emphasize the importance of strategic sensor placement in geometrically complex areas.

It is worth noting that while polycarbonate is employed for the numerical model in this study to facilitate the observation of distinct strain responses, the underlying formulation of the proposed virtual sensing algorithm is based on linear elastic principles. Therefore, the fundamental logic and mathematical consistency of the method remain valid regardless of the specific material properties, such as those of aluminum or composite materials typically used in aerospace structures, provided the response remains within the elastic regime. Consequently, the proposed virtual sensing method shows great promise for structural health monitoring by enabling continuous full-field deformation monitoring.

Future research will focus on wind tunnel experiments to validate the algorithm using physically measured data. Subsequent studies will also aim to address practical implementation challenges, such as compensating for thermal strain and measurement noise under real-world flight environments. While the current framework was specifically validated under symmetric, quasi-static cruise conditions to verify the numerical stability of the algorithm across varying load magnitudes, actual flight operations involve spatially complex, asymmetric loading scenarios. Therefore, extending the present methodology to handle combined bending-torsion responses, such as those induced by roll maneuvers, asymmetric gusts, or varying angles of attack, through full dynamic analyses remains a critical direction for future research to further demonstrate the robustness and practical applicability of the proposed technique. Furthermore, conducting comprehensive benchmark studies against alternative methodologies, such as Kalman filter-based approaches and the inverse finite element method (iFEM), will be essential to comparatively evaluate computational efficiency and accuracy under dynamic conditions.

Acknowledgements

This research was supported by Basic Science Research Program through the National Research Foundation of Korea (NRF) funded by the Ministry of Education (RS-2022-NR070875). This research was supported by the Regional Innovation System & Education (RISE) program through the Gyeonggi RISE Center, funded by the Ministry of Education and the Gyeonggi Province, Republic of Korea (2025-RISE-09-A38). This work was also supported by the Aviation and Drone Convergence University project, funded by the Ministry of Education. The authors would also like to express their gratitude to Professor Moonsung Cho from Korea Aerospace University for providing the CAD model of the BWB aircraft.

References

1. Farrar, C.R., Worden, K. (2012). Structural health monitoring: a machine learning perspective. John Wiley & Sons, Hoboken, NJ, USA.
2. Liu, Y., Nayak, S. (2012). Structural health monitoring: state of the art and perspectives. Jom, 64(7), 789-792. https://doi.org/10.1007/s11837-012-0370-9.
3. Gharehbaghi, V.R., Noroozinejad Farsangi, E., Noori, M., Yang, T.Y., Li, S., Nguyen, A., Mirjalili, S. (2022). A critical review on structural health monitoring: definitions, methods, and perspectives. Archives of Computational Methods in Engineering, 29(4), 2209-2235. https://doi.org/10.1007/s11831-021-09665-9.
4. Martinez-Luengo, M., Kolios, A., Wang, L. (2016). Structural health monitoring of offshore wind turbines: a review through the statistical pattern recognition paradigm. Renewable and Sustainable Energy Reviews, 64, 91-105. https://doi.org/10.1016/j.rser.2016.05.085.
5. Sohn, H. (2007). Effects of environmental and operational variability on structural health monitoring. Philosophical Transactions of the Royal Society A: Mathematical, Physical and Engineering Sciences, 365(1851), 539-560. https://doi.org/10.1098/rsta.2006.1935.

6. Boller, C. (2000). Next generation structural health monitoring and its integration into aircraft design. International Journal of Systems Science, 31(11), 1333-1349. https://doi.org/10.1080/00207720050197730.
7. Grieves, M., Vickers, J. (2016). Digital twin: Mitigating unpredictable, undesirable emergent behavior in complex systems. Transdisciplinary perspectives on complex systems: new findings and approaches, 85-113. https://doi.org/10.1007/978-3-319-38756-7_4.
8. Gherlone, M., Cerracchio, P., Mattone, M., Di Sciuva, M., Tessler, A. (2012). Shape sensing of 3D frame structures using an inverse finite element method. International Journal of Solids and Structures, 49(22), 3100-3112. https://doi.org/10.1016/j.ijsolstr.2012.06.009.
9. Kefal, A., Oterkus, E. (2016). Displacement and stress monitoring of a chemical tanker based on inverse finite element method. Ocean Engineering, 112, 33-46. https://doi.org/10.1016/j.oceaneng.2015.11.032.
10. Mora, B., Basurko, J., Leturiondo, U., Albizuri, J. (2021). Kalman-based virtual sensing for structural health monitoring, Proceedings of the DinEst, July, Spain.
11. Peng, Z., Dong, K., Yin, H. (2019). A modal-based Kalman filter approach and OSP method for structural response reconstruction. Shock and Vibration, 2019(1), 5475686. https://doi.org/10.1155/2019/5475686.
12. Shin, S., Hyun, C., Cho, S., Lee, P.S. (2023). Multi-sensor data-based anomaly detection and diagnosis of a pumped storage hydropower plant. Structural Engineering and Mechanics, 88(6), 569-581. https://doi.org/10.12989/sem.2023.88.6.569.
13. Cho, S., Kim, S.W., Kim, H.J. (2024). Fault detection in blade pitch systems of floating wind turbines utilizing transformer architecture. Structural Engineering and Mechanics, 92(2), 121-131. https://doi.org/10.12989/sem.2024.92.2.121.
14. Ihn, J.B., Chang, F.K. (2004). Detection and monitoring of hidden fatigue crack growth using a built-in piezoelectricsensor/actuator network: I. diagnostics. Smart Materials and Structures, 13(3), 609. https://doi.org/10.1088/0964-1726/13/3/020.
15. Ihn, J. B., Chang, F.K. (2004). Detection and monitoring of hidden fatigue crack growth using a built-in piezoelectricsensor/actuator network: II. validation using riveted joints and repair patches. Smart Materials and Structures, 13(3), 621. https://doi.org/10.1109/JSEN.2022.3212070.
16. Giurgiutiu, V. (2014). Structural health monitoring with piezoelectric wafer active sensors. Academic Press.
17. Lee, J., Ki, S., Kim, S., Shin, Y., Cho, S.P. (2025). Optimization of fan blade cross-sections for improved fatigue life and weight reduction. Structural Engineering and Mechanics, 94(4), 313-324. https://doi.org/10.12989/sem.2025.94.4.313.
18. Skafte, A., Kristoffersen, J., Vestermark, J., Tygesen, U.T., Brincker, R. (2017). Experimental study of strain estimation on wave induced structures using modal decomposition and quasi static Ritz vectors. Engineering Structures, 136, 261-276. https://doi.org/10.1016/j.engstruct.2017.01.014.
19. Kullaa, J. (2019). Bayesian virtual sensing in structural dynamics. Mechanical Systems and Signal Processing, 115, 497-513. https://doi.org/10.1016/j.ymssp.2018.06.010.
20. Mora, B., Basurko, J., Sabahi, I., Leturiondo, U., Albizuri, J. (2023). Strain virtual sensing for structural health monitoring under variable loads. Sensors, 23(10), 4706. https://doi.org/10.3390/s23104706.
21. Jia, J., Li, Y. (2023). Deep learning for structural health monitoring: data, algorithms, applications, challenges, and trends. Sensors, 23(21), 8824. https://doi.org/10.3390/s23218824.
22. Samy, I., Postlethwaite, I., Gu, D.W. (2011). Survey and application of sensor fault detection and isolation schemes. Control Engineering Practice, 19(7), 658-674. https://doi.org/10.1016/j.conengprac.2011.03.002.
23. Nabiyan, M.S., Khoshnoudian, F., Moaveni, B., Ebrahimian, H. (2021). Mechanics-based model updating for identification and virtual sensing of an offshore wind turbine using sparse measurements. Structural Control and Health Monitoring, 28(2), e2647. https://doi.org/10.1002/stc.2647.
24. Kullaa, J. (2017). Development of virtual sensors to increase the sensitivity to damage. Procedia Engineering, 199, 1937-1942. https://doi.org/10.1016/j.proeng.2017.09.290.
25. Kong, C., Zhao, D., Zhang, J., Liang, B. (2022). Real-time virtual sensing for dynamic vibration of

flexible structure via fiber Bragg grating sensors. IEEE Sensors Journal, 22(22), 21706-21718. https://doi.org/10.1109/JSEN.2022.3212070.
26. Yan, J., Cheng, Y., Zhang, L., Li, Z., Xu, T., Zhang, F., Sui, Q. (2023). Displacement field reconstruction technique for plate-like structures based on model superposition method. Measurement and Control, 56(3-4), 654-667. https://doi.org/10.1177/00202940221095535.
27. Yu, M., Guo, J., Lee, K.M. (2018). A modal expansion method for displacement and strain field reconstruction of a thin-wall component during machining. IEEE/ASME Transactions on Mechatronics, 23(3), 1028-1037. https://doi.org/10.1109/TMECH.2018.2790922
28. Lee, S., Park, M., Oh, M., Lee, P.S. (2024). Virtual sensing for real-time strain field estimation and its verification on a laboratory-scale jacket structure under water waves. Computers & Structures, 298, 107344. https://doi.org/10.1016/j.compstruc.2024.107344.
29. Ferhatoglu, E., Cigeroglu, E., Özgüven, H.N. (2018). A new modal superposition method for nonlinear vibration analysis of structures using hybrid mode shapes. Mechanical Systems and Signal Processing, 107, 317-342. https://doi.org/10.1016/j.ymssp.2018.01.036.
30. Zhang, Y., Zhou, J., Shi, L., Cui, B. (2024). Design optimization for the entire aircraft structure of civil aircraft with blended-wing-body layout. Structural and Multidisciplinary Optimization, 67(6), 106. https://doi.org/10.1007/s00158-024-03820-z.
31. Ahuja, J., Perron, C., Rivera, R.B., Tai, J.C., Mavris, D.N. (2025). Comparison of blended wing body and tube-and-wing performance characteristics. The Aeronautical Journal, 129(1337), 1764-1790. https://doi.org/10.1017/aer.2025.8.
32. Dakka Dr, S., Johnson, O. (2019). Aerodynamic design and exploration of a blended wing body aircraft at subsonic speed. International Journal of Aviation, Aeronautics, and Aerospace, 6(5), 17. https://doi.org/10.15394/ijaaa.2019.1411.
33. Ock, S., Cho, M.S. (2025). Blended wing body aircraft shape design and automation. M.S. Dissertation, Korea Aerospace University, Goyang, Korea.
34. Lee, B., Kim, H., Kim, M.S. (2012). Aerodynamics. Sehwa Publishing, Seoul, Korea.
35. Reist, T.A., Zingg, D.W. (2016). Aerodynamic design of blended wing-body and lifting-fuselage aircraft. 34th AIAA Applied Aerodynamics Conference, 3874. https://doi.org/10.2514/6.2016-3874.
36. Qin, N., Vavalle, A., Le Moigne, A. (2005). Spanwise lift distribution for blended wing body aircraft. Journal of Aircraft, 42(2), 356-365. https://doi.org/10.2514/1.4229.